I&EC research
Industrial & Engineering Chemistry Research

pubs.acs.org/IECR

Article

Efficient Electrochemical Reduction of CO_2 to CO by Ag-Decorated B-Doped g-C_3N_4: A Combined Theoretical and Experimental Study

Song Lu, Yang Zhang, Mohamed F. Mady, Wakshum Mekonnen Tucho, Fengliu Lou,* and Zhixin Yu*

Cite This: https://doi.org/10.1021/acs.iecr.2c00152

Read Online

ACCESS | Metrics & More | Article Recommendations | Supporting Information

ABSTRACT: Electrochemical CO_2 reduction (ECR) has received great attention in energy conversion and CO_2 mitigation. In recent years, graphitic carbon nitride (g-C_3N_4) has been regarded as a very promising support for metal nanoparticles (NPs) for many catalytic reactions. In this work, we reported the silver- (Ag) loaded boron-doped g-C_3N_4 nanocomposite (Ag-B-g-C_3N_4) for efficient ECR to CO by a joint first-principles study and experimental work. Theoretical simulation demonstrated that the B dopant and Ag NPs could be easily incorporated into g-C_3N_4. The introduction of Ag NPs and the B atom could greatly decrease the adsorption free energy for the *COOH intermediate generation. Meanwhile, an electron-rich region at the Ag-B-g-C_3N_4 interface was observed, contributing to improved electrical conductivity and electron transport. B-g-C_3N_4 could not exhibit the obvious enhancement of ECR performance, while the Ag-B-g-C_3N_4 catalyst with an average Ag diameter of 4.95 nm exhibited a total current density of 2.08 mA cm^{-2} and a CO Faradaic efficiency (FE_{CO}) of 93.2% under the potential of −0.8 V vs the reversible hydrogen electrode (RHE), indicating that Ag is the only active center. Ag-B-g-C_3N_4 also displayed excellent stability without any deactivation in a 12-h electrocatalysis. This work revealed the mechanism of electrocatalytic CO_2 reduction over metal- (Ag) and nonmetal- (B) modified g-C_3N_4, which paves the way for broader application of the g-C_3N_4 nanocomposite in electrocatalytic reactions.

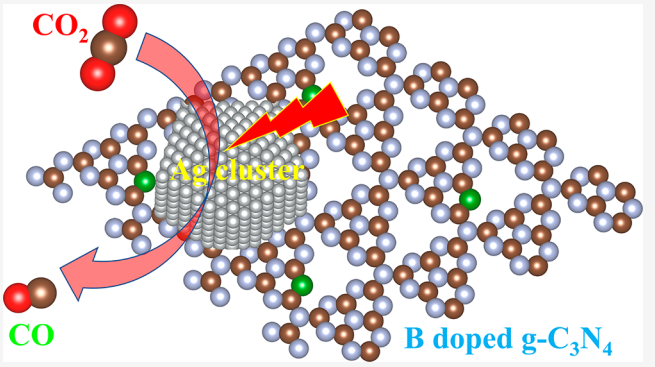

INTRODUCTION

Over the past decades, the huge consumption of fossil energy and the dramatic rise in atmospheric CO_2 concentration have led to various issues such as an energy crisis and global warming. Converting CO_2 to value-added chemicals and fuels has been considered as an effective approach to mitigate the above dilemma.[1,2] Among which, electrochemical CO_2 reduction (ECR) shows several advantages.[3,4] ECR can be proceeded under ambient temperatures and pressures. Besides, the required electricity input can be produced by wind, solar, and tidal energy. More importantly, a diverse range of products can be formed by tuning the external potentials and other reaction parameters.[5] Nevertheless, the activation of the CO_2 molecule is quite difficult because it requires an energy of 803 kJ/mol to break the C═O bond.[6,7] In addition, as the competitive hydrogen evolution reaction (HER) and multi-proton coupled electron transfer commonly take place, ECR suffers low selectivity toward specific products.[8,9] To date, carbon- and metal-based materials have been widely explored and demonstrated as effective electrocatalysts in ECR.[10−13] Shi et al. used the Au/C electrode to investigate the role of wettability in ECR.[14] They suggested that CO_2 concentration of the interfaces could influence ECR efficiency under high current densities. Carbon-supported single-atom catalysts (SACs) have been widely investigated, as they demonstrated outstanding performance in ECR to CO. For instance, a Ni SAC exhibits a 98.9% CO Faradaic efficiency (FE_{CO}) at −1.2 V.[15] It has been reported that Ag can be a good candidate for ECR to CO due to its relatively weak binding energy to the *CO intermediate.[16] Nevertheless, Ag-based catalysts generally show sluggish kinetics in ECR. Meanwhile, the stability and selectivity are not satisfactory. Therefore, the design of high-performance Ag-based electrocatalysts for ECR application is of interest.

Recently, loading metal nanoparticles (NPs) on two-dimensional (2D) materials as catalysts has gained intensive attention.[17−20] It is worth noting that 2D organic semiconductor graphitic carbon nitride (g-C_3N_4) possesses sp^2 hybridization of C and N atoms that form the π-conjugated graphitic plane, exhibiting excellent stability in a variety of catalytic reactions.[21−23] Besides, g-C_3N_4 also possesses other merits such as high surface area, low cost, and easy preparation,

Special Issue: Engineered Methodologies for CO2 Utilization

Received: January 12, 2022
Revised: March 7, 2022
Accepted: March 10, 2022

which enables it to be an ideal molecular scaffold for engineering metal NPs for excellent performance in multiple electrocatalytic applications.[12,24,25] Especially, the existence of pyridinic nitrogen atoms and high oxophilicity C atoms will boost the interaction between the catalysts and reactants/intermediates such as *COOH and *CO in ECR.[26,27] Zhang et al. reported that g-C_3N_4-supported gold (Au) NPs exhibit better ECR activity than carbon-supported Au NPs, achieving a FE_{CO} above 90% in a wide potential window between −0.45 and −0.85 V vs a reversible hydrogen electrode (vs RHE).[28] Density functional theory (DFT) calculations evidenced that the interaction between Au and g-C_3N_4 induces the generation of negative charges on the Au surface, promoting the generation of key intermediates. Recently, studies demonstrated that doping nonmetal atoms to modify the g-C_3N_4 support has positive effects on the overall ECR activity. For instance, Ag NP-loaded S-decorated g-C_3N_4/CNT exhibits a FE_{CO} of over 90% under −0.77 V (vs RHE) with a high current density of 21.3 mA cm^{-2}. Theoretical calculations revealed that S atoms could increase the electron density of the Ag-loaded g-C_3N_4 interface, promoting CO_2 molecule activation.[29] In other words, effective interfacial electron transfer between support and NPs could improve catalytic activity. Meanwhile, doping nonmetal atoms into the framework can change its electronic structures, while the modified framework could serve as a better support for metal NP deposition and to activate metal NPs.

A previous study had also indicated that boron- (B) modified g-C_3N_4 (B-g-C_3N_4) could effectively alter its electronic structures and improve its performance in various reactions.[30,31] Nevertheless, there is little research on B-g-C_3N_4 as a substrate for NPs used in ECR, while we can envisage that NPs-B-g-C_3N_4 hybrid nanomaterials could exhibit excellent ECR performance. In this work, we chose Ag NPs for the preparation of the Ag-B-g-C_3N_4 composite for ECR. We first investigated the geometric configurations, formation energies, and electronic structures of g-C_3N_4, B-g-C_3N_4, and Ag-B-g-C_3N_4 by first-principles calculation to predict their ECR performance. Our simulation results suggested that the composite electrocatalyst could show excellent stability, electronic conductivity, and low free energy barrier for the generation of the *COOH intermediate. The corresponding ECR to the CO mechanism on these three electrocatalysts was studied by calculating the adsorption free energy of each step, indicating that the generation of *COOH is the potential determining step. Thereafter, we prepared the three electrocatalysts for experimental verification. Only Ag-decorated B-g-C_3N_4 could reduce CO_2 to CO, while the other two catalysts only produced H_2. Meanwhile, no liquid product was detected. The Ag-B-g-C_3N_4 catalyst displayed the maximum FE_{CO} of 93.2% under a potential of −0.8 V (vs RHE) with a total current density of 2.08 mA cm^{-2}. It also exhibited excellent stability, as evidenced by negligible decay after a 12-h ECR activity test.

SIMULATION

All calculations in this work were conducted by using plane-wave DFT implemented in the Vienna ab initio simulation package (VASP).[32,33] The electronic exchange-correlation energy was treated by the Perdew−Burke−Ernzerhof (PBE) functional within the generalized gradient approximation (GGA).[34,35] The projector augmented wave (PAW) method with a cutoff energy of 500 eV was used to describe the ionic cores. In the z direction, the thickness of the vacuum was set to 20 Å to avoid periodic interactions. We chose a 4 × 4 × 1 k-point grid for structure optimization, and an 8 × 8 × 1 k-point grid for electronic structure calculations. The convergence criterion of the energy and force were 10^{-5} eV and 10^{-2} eV/Å. To better describe the dispersion interaction from molecules, the vdW correction was included by Grimme's scheme (DFT-D3).[36]

The substituted energy (E_{sub}) of B-g-C_3N_4 can be used to estimate its thermal stability by the following equation

$$E_{sub} = E(\text{doped}) - E(\text{g-}C_3N_4) + \mu(\text{N}) - \mu(\text{B}) \quad (1)$$

where E(doped) and E(g-C_3N_4) are the energy of the B-modified and pristine g-C_3N_4 monolayers, while μ(N) and μ(B) are the energy of N and B atoms from the reference phase.

The adsorption energy of the Ag cluster can be calculated by the equation below

$$E_{ads} = E(\text{Ag-B-g-}C_3N_4) - E(\text{Ag}_4\text{ cluster}) - E(\text{B-g-}C_3N_4) \quad (2)$$

where E(Ag-B-g-C_3N_4), E(Ag_4 cluster), and E(B-g-C_3N_4) denote the energy of the Ag_4 cluster loaded on B-g-C_3N_4, the Ag_4 cluster, and B-g-C_3N_4, respectively.

Based on the computational hydrogen electrode (CHE) model,[37] the chemical potential of H_2 (g) can be equal to $\mu(H^+ + e^-) = 1/2\mu(H_2)$. The Gibbs free energy change for adsorbates can be expressed as $\Delta G = \Delta E + \Delta E_{ZPE} - T\Delta S$, where E is the electronic energy from the DFT calculation, ZPE and TS are the zero-point energy and entropy correction, and T is the temperature which is set to be 298.15 K.

The adsorption and desorption of intermediates for CO generation can be expressed as below

$$* + CO_2 + (H^+ + e^-) \rightarrow *\text{COOH} \quad (3)$$

$$*\text{COOH} + (H^+ + e^-) \rightarrow *\text{CO} + H_2O \quad (4)$$

$$*\text{CO} \rightarrow \text{CO} + * \quad (5)$$

where * denotes the catalytic site.

EXPERIMENTAL SECTION

Chemicals. All chemicals are analytical reagents and used as-received without further purification. Deionized water generated by a Milli-Q (18.2 MΩ cm) system was used in all experiments. Silver nitrate ($AgNO_3$), boric acid (H_3BO_3), and sodium borohydride ($NaBH_4$) were ordered from Sigma-Aldrich. Trisodium citrate ($C_6H_5Na_3O_7$), potassium bicarbonate ($KHCO_3$), Nafion D-521 dispersion, Nafion-117 ionic exchange membrane, and urea ($CO(NH_2)_2$) were purchased from Alfa Aesar. Hydrogen peroxide (H_2O_2) and sulfuric acid (H_2SO_4) were bought from VWR. Carbon paper was purchased from Toray.

Pretreatment of the Ionic Exchange Membrane and Carbon Paper. The Nafion-117 membrane was boiled in a 5 wt % H_2O_2 aqueous solution at 80 °C for 1 h to remove organic impurities in the membrane. The membrane was rinsed repeatedly with deionized water, soaked in deionized water at 80 °C, and further boiled for 1 h to completely remove residual H_2O_2. The membrane was then boiled again in a H_2SO_4 (1.0 M) solution at 80 °C for 1 h. Finally, the membrane was rinsed repeatedly with deionized water and immersed in deionized water at 80 °C for 1 h to completely

https://doi.org/10.1021/acs.iecr.2c00152
Ind. Eng. Chem. Res. XXXX, XXX, XXX−XXX

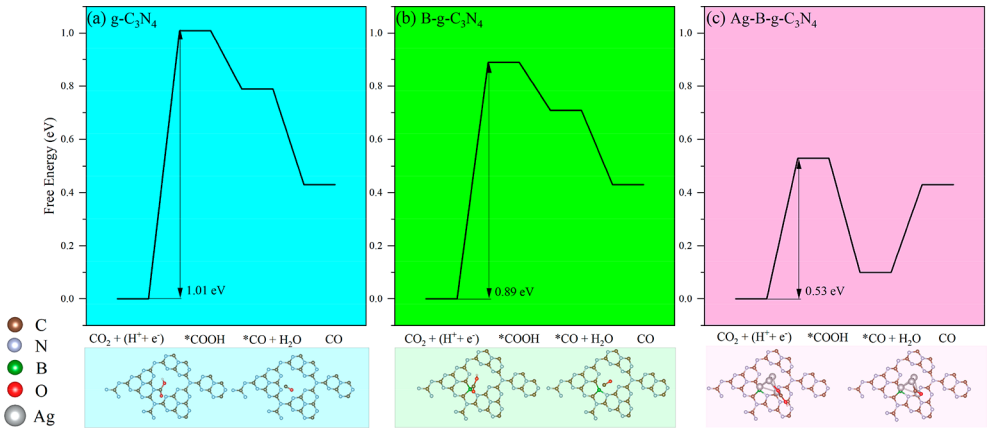

Figure 1. Calculated free energy profiles for ECR to CO on (a) g-C_3N_4, (b) B-g-C_3N_4, and (c) Ag-B-g-C_3N_4. The adsorption structures of key intermediates *COOH and *CO are depicted below.

remove the residual H_2SO_4. The carbon paper was immersed in an ethanol solution, ultrasonicated for 5 min, and then dried vacuum at 60 °C for 12 h before use.

Synthesis of Electrocatalysts. For the synthesis of g-C_3N_4, 20 g of $CO(NH_2)_2$ was put into a covered crucible, heated to 600 °C with a ramp rate of 5 °C min^{-1}, and kept for 2 h in the muffle furnace. After cooling to room temperature, the g-C_3N_4 sample was obtained. The sample was further sonicated in deionized water for 2 h to obtain a thin g-C_3N_4 nanosheet.

For the synthesis of B-doped g-C_3N_4, the mixture of 20 g of $CO(NH_2)_2$ and 0.3 g of H_3BO_3 was ground evenly and placed in a covered crucible. The crucible was heated to 600 °C with a ramp rate of 5 °C min^{-1} and held at 600 °C for 2 h in a muffle furnace. After cooling down, the sample was washed with hot water in order to remove B_2O_3 and then vacuum dried for 24 h at 60 °C. The as-prepared B-g-C_3N_4 sample was sonicated for 2 h to obtain a thin nanosheet.

The loading of Ag NPs on B-g-C_3N_4 was performed according to a procedure from a previous study.[28] Typically, 1.176 g of $Na_3C_6H_5O_7$ and 0.085 g of $AgNO_3$ were dissolved in 300 mL of deionized water under a dark environment. Then, the mixture of 0.081 g of B-g-C_3N_4 and the above solution was sonicated for 1 h. Subsequently, 50 mL of a 0.05 M $NaBH_4$ solution was added dropwise under vigorous stirring for 8 h. The sample was collected by centrifugation, washed with deionized water, and finally vacuum dried at 60 °C overnight. The Ag loading was 13.9 wt % based on inductively coupled plasma optical emission spectroscopy (ICP-OES).

Electrocatalyst Characterization. The structures of the electrocatalysts were investigated by an X-ray diffractometer (Bruker-AXS Microdiffractometer D8 ADVANCE) with a CuKα radiation source (λ = 1.54 Å) at a scan rate of 3° min^{-1}. The morphologies were examined by transmission electron microscopy (TEM) and high-resolution transmission electron microscopy (HRTEM, JEOLJEM-2100F, 200 kV). The surface compositions and element states of the catalysts were tested by X-ray photoelectron spectroscopy (XPS, ESCALAB Xi^+) using Al Kα excitation at 1486.6 eV.

Electrochemical Measurement. The electrocatalytic CO_2 reduction was carried out in a three-electrode sealed H-type cell consisting of a working electrode (carbon paper, CP), a reference electrode (saturated Ag/AgCl (3 M KCl)), and a counter electrode (Pt (1 cm^2)). All potentials were controlled by the AUTOLAB PGSTAT302N workstation and converted to RHE by E (vs RHE) = E (vs Ag/AgCl) + 0.197 V + 0.059 × pH. For each experiment, the mixture of 1 mg of the catalyst and 1 mg of carbon black was dispersed in a solution containing 500 μL of ethanol, 440 μL of H_2O, and 60 μL of a 0.5 wt % Nafion-D521 solution by sonication for 90 min. Then, 100 μL of the electrocatalyst ink was dropped uniformly on a piece of CP (1 × 2 cm) as the working electrode, followed by drying under an infrared lamp for 30 min. The area of the electrocatalyst was controlled to 1 cm^2 with a loading of 0.1 mg cm^{-2}. The Nafion-117 membrane was used to separate the anode and cathode chambers. The pH value of the 0.5 M $KHCO_3$ electrolyte is 7.2. High purity CO_2 was bubbled into the cathode chamber at a flow rate of 20 mL min^{-1} for 1 h before and during the test. Meanwhile, the electrolyte in the cathode was stirred at 1200 rmp. The linear sweep voltammetry (LSV) was collected in 0.5 M $KHCO_3$ at a scan rate of 10 mV s^{-1}. Electrochemical impedance spectroscopy (EIS) was measured in 0.5 M $KHCO_3$ at −0.8 V (vsRHE) with an amplitude of 5 mV from 10^{-2} to 10^{-5} Hz.

Gaseous products CO and H_2 were quantified by an online gas chromatograph (GC, Agilent 7890B) with two TCD detectors equipped with a HayeSep Q column and a 5A molecular sieve column. Liquid products were determined by nuclear magnetic resonance (NMR) spectroscopy with a 400 MHz Bruker NMR spectrometer. The FE of gaseous products under different potentials was calculated by the equation below

$$FE = (Z \times P \times F \times V \times \nu)/(R \times T \times I) \quad (6)$$

where Z is the number of transferred electrons for one CO_2 molecule reduction to the gaseous product, which is 2 for CO and H_2; P is the atmospheric pressure of 1.01×10^5 Pa; F is the Faraday constant 96485 C mol^{-1}; V is the gas flow rate; ν is the volumetric concentration of the gas product; T is the temperature of 298.15 K; R is the ideal gas constant 8.314 J mol^{-1} K^{-1}; and I is the steady-state current at each applied potential.

RESULTS AND DISCUSSION

DFT Results. There are three different N atoms (N1, N2, and N3 sites) and two different C atoms (C1 and C2 sites) in g-C_3N_4, as shown in Figure S1. Previous studies have demonstrated that the N2 atom with a low coordination number is preferable to be substituted by nonmetal atoms.[30,31] Therefore, the B-doped g-C_3N_4 monolayer was built with one B atom substituting for one N2 atom. After geometric

https://doi.org/10.1021/acs.iecr.2c00152
Ind. Eng. Chem. Res. XXXX, XXX, XXX−XXX

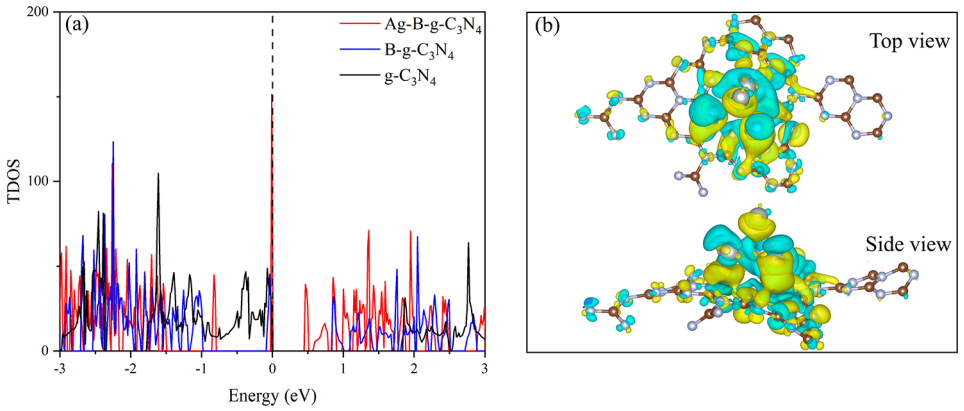

Figure 2. (a) Total density of states (TDOS) of g-C_3N, B- g-C_3N_4, and Ag-B-g-C_3N_4, where Fermi energy locates at 0 eV. (b) Charge density difference between Ag NPs and B-g-C_3N_4 for Ag-B-g-C_3N_4, where yellow and cyan denote electron accumulation and depletion, respectively. The isosurface value is set to be 0.001 e/Bohr^3.

optimization, the B atom bonds with the nearest N2 atom and C1 atom, forming pentagonal and hexagonal rings. The E_{sub} of B-doped g-C_3N_4 is −1.38 eV, indicating the ease of introducing the B atom into the g-C_3N_4 skeleton. The E_{ads} of the Ag cluster on B-g-C_3N_4 is −1.98 eV, demonstrating that the Ag_4 cluster is loaded stably on the B-g-C_3N_4 support, and the resulting composite catalyst could possess good stability.

The calculated Gibbs free energy change (ΔG) of the intermediates on g-C_3N_4, B-g-C_3N_4, and Ag-B-g-C_3N_4 was displayed in Figure 1a–c. The formation of intermediate *COOH is the potential determining step on the three electrocatalysts. The free energy barrier for CO production on pristine g-C_3N_4 is quite large at 1.01 eV, while the free energy barrier decreases by only 0.12 eV after introducing B atoms, indicating the B atom alone cannot effectively improve the ECR performance. However, the combination of B and Ag atoms shows a large drop in the free energy barrier of 0.53 eV, which suggested that the B dopant and Ag NPs could be promising to enhance the ECR performance of g-C_3N_4. We further considered the possible active sites after the doping of B and Ag, including S1 (B atom), S2 (N atom), S3 (C atom), S4 (N atom), S5 (N atom), and S6 (C atom) around the Ag cluster (Figure S2a). It turns outs that the intermediates could not be adsorbed on S1, S2, S3, S4, and S6. Only S5 can be a stable adsorption site for intermediates but with a free energy barrier of 1.16 eV (Figure S2b), larger than that of the Ag site. Thus, B, C, and N atoms will not be the active sites for CO_2 activation, and the Ag cluster is the only active center. The adsorption configurations of *COOH and *CO intermediates on the three electrocatalysts suggest that *COOH could bond with N, B, and Ag atoms with different strengths, leading to uphill Gibbs free energy. In contrast, *CO could not bond well with the N and B atoms, exhibiting an exothermic nature for CO desorption from pristine and B-doped g-C_3N_4. However, it could interact strongly with Ag atoms, resulting in an endothermic reaction for CO desorption.

We further investigated the electronic structures of Ag-B-g-C_3N_4 by calculating the total density of states, Bader charge, and charge density difference. It is worth noting that there are more electron states between the conduction band and valence band and even near the Fermi level in B and Ag-modified g-C_3N_4 (Figure 2a). In other words, the introduction of B atoms and the Ag cluster could induce more impurity levels, which could improve the electrical conductivity and increase the ECR activity. Besides, the detailed charge transfer between B, Ag, and g-C_3N_4 was shown in Figure 2b. The B atom transferred 1.71 e to C and N atoms, while the total charge transfer from the Ag cluster to the B-g-C_3N_4 scaffold is 0.74 e, contributing to an electron-rich region at the interface of Ag and B-g-C_3N_4. It can be proposed that the B dopant could improve electrical conductivity of the g-C_3N_4 support, while Ag NPs could sever as the ECR active center. Therefore, we synthesized the three catalysts (g-C_3N_4, B-g-C_3N_4, and Ag-B-g-C_3N_4) to verify the role of B and Ag NPs as proposed by DFT simulations.

Electrocatalyst Characterization. To evidence the formation of nanocomposites, crystal structures were investigated by XRD characterization (Figure 3). Two characteristic

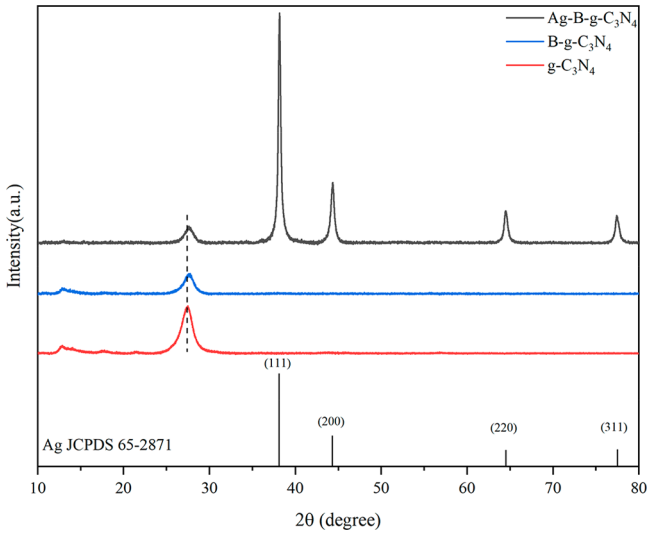

Figure 3. XRD patterns of g-C_3N_4, B-g-C_3N_4, and Ag-B-g-C_3N_4.

peaks located at 13.0° (100) and 27.6° (002) are assigned to the in-plane structure of tri-*s*-triazine motifs and the periodic stacking of layers of conjugated aromatic rings.[38,39] The slight shift of the (002) peak toward the high angle for B-g-C_3N_4 and Ag-B-g-C_3N_4 was probably related to structural variations such as the decreased interlayer distance after introducing B atoms.[40] The gradual decrease of the characteristic peak of g-C_3N_4 could be explained by the less ordered structure and reduced crystallinity after the doping of B and Ag. The XRD result could be supported by the structure deformation after introducing B and Ag NPs from the DFT simulation study

https://doi.org/10.1021/acs.iecr.2c00152
Ind. Eng. Chem. Res. XXXX, XXX, XXX−XXX

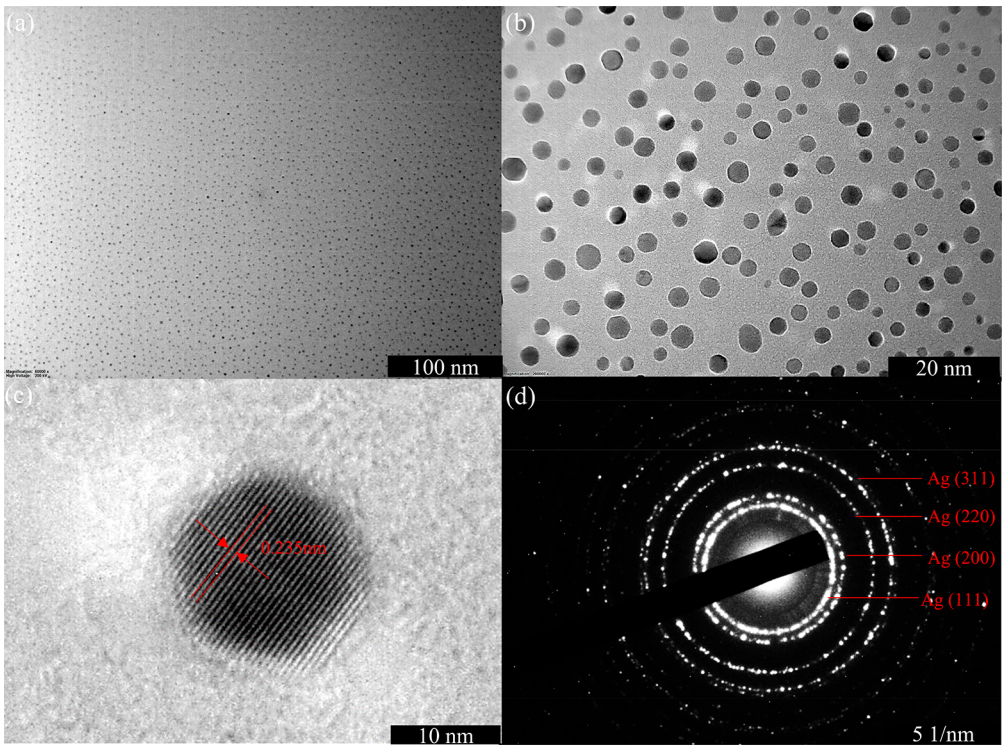

Figure 4. (a) and (b) TEM images of Ag-B-g-C_3N_4 with different magnifications. (c) HRTEM image of Ag-B-g-C_3N_4, which shows an interlayer distance of 0.235 nm for Ag. (d) SAED pattern of Ag NPs.

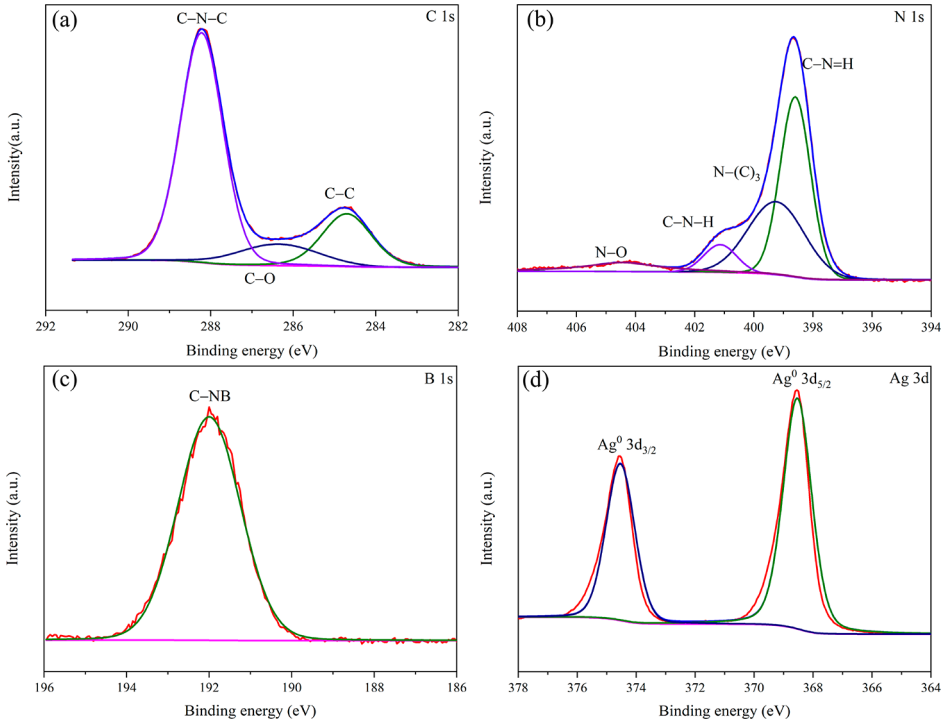

Figure 5. XPS spectra of Ag-B-g-C_3N_4 (a) C 1s, (b) N 1s, (c) B ls, and (d) Ag 3d.

(Figure S1). Diffraction peaks located at 2θ = 38.1°, 44.3°, 64.4°, and 77.4° are the characteristic peaks of (111), (200), (220), and (311) crystal planes of Ag (Joint Committee for Powder Diffraction Standards (JCPDS) No. 65-2871). Meanwhile, the main characteristic peak of the B-g-C_3N_4 support was maintained. In addition, diffraction peaks of B_2O_3 or Ag_2O were not observed. Therefore, metallic Ag NP-loaded B-doped g-C_3N_4 (Ag-B-g-C_3N_4) was successfully prepared.

TEM was employed to study the morphology and size of Ag-B-g-C_3N_4. As exhibited in Figure 4a,b, spherical Ag NPs were evenly deposited on the B-g-C_3N_4. The average diameter of NPs is 4.95 nm, as further exemplified by TEM images in Figure S3, where the particle size distribution was also shown.

https://doi.org/10.1021/acs.iecr.2c00152
Ind. Eng. Chem. Res. XXXX, XXX, XXX−XXX

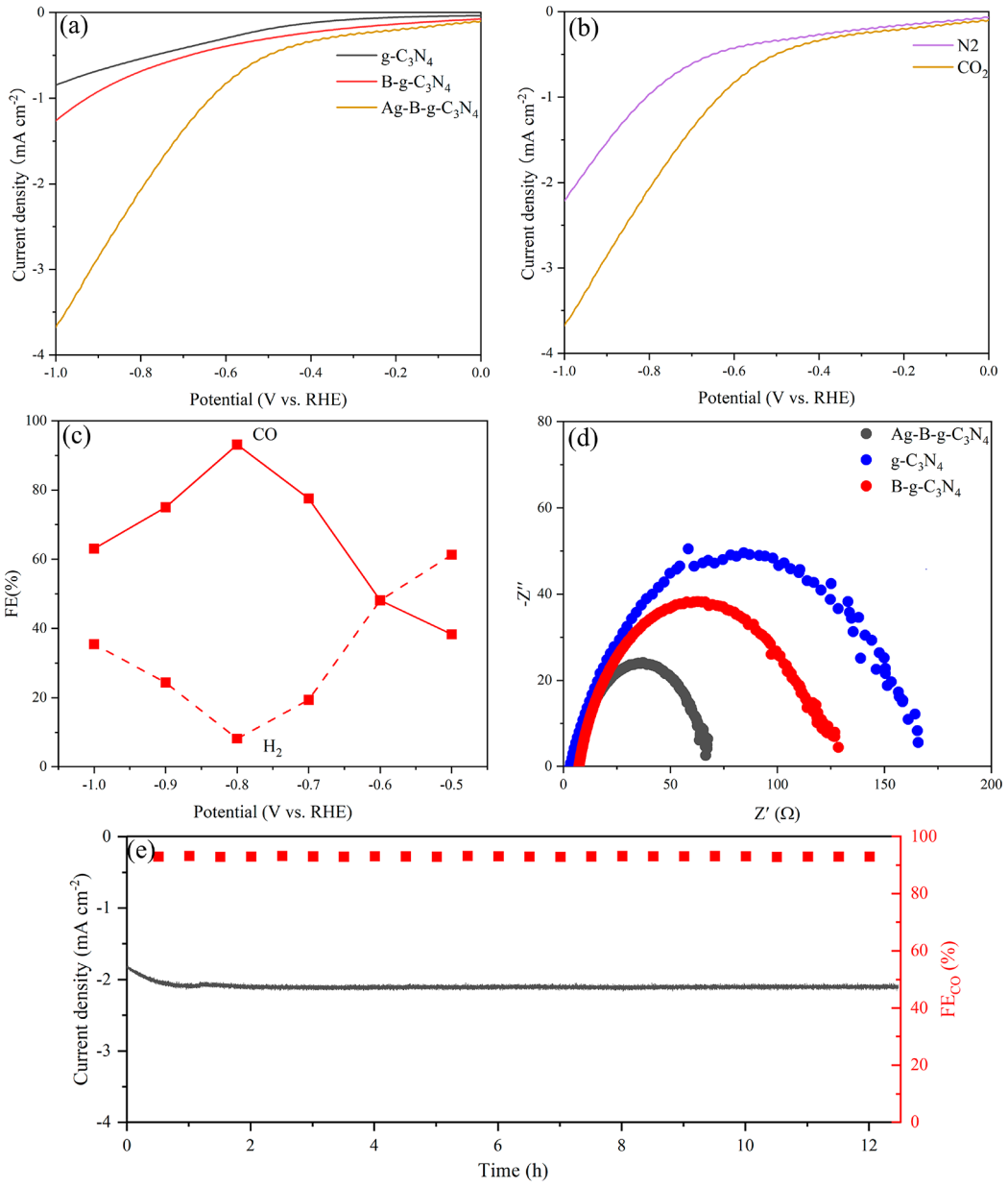

Figure 6. (a) LSV curves of g-C_3N_4, B-g-C_3N_4, and Ag-B-g-C_3N_4 catalysts in a CO_2-saturated 0.5 M $KHCO_3$ solution at a scan rate of 10 mV s^{-1}. (b) LSV curves of the Ag-B-g-C_3N_4 catalyst in N_2- and CO_2-saturated 0.5 M $KHCO_3$ solutions at a scan rate of 10 mV s^{-1}. (c) The Faradaic efficiencies of CO generation and H_2 generation on the Ag-B-g-C_3N_4 catalyst. (d) EIS Nyquist plots for g-C_3N_4, B-g-C_3N_4, and Ag-B-g-C_3N_4 catalysts in 0.5 M $KHCO_3$ under the potential of −0.8 V (vs RHE). (e) Stability test of the Ag-B-g-C_3N_4 catalyst in 0.5 M $KHCO_3$ under −0.8 V (vs RHE) for 12 h.

It can be clearly seen that an interplanar spacing of 0.235 nm was obtained from the lattice fringes for Ag NPs (Figure 4c), attributing to the (111) plane of metallic Ag and close to the theoretical value of 0.236 nm. The selected area electron diffraction pattern (SAED) of Ag-B-g-C_3N_4 was shown in Figure 4d. The diffraction circles corresponding to the (111), (200), (220), and (311) planes of Ag are apparent, consistent with the XRD results.

The high-resolution XPS spectra of C 1s, N 1s, B 1s, and Ag 3d levels for Ag-B-g-C_3N_4 are shown in Figure 5a−d. As the samples have been calcinated in air, O atoms would be inevitably introduced into the skeletons. Therefore, C−O and N−O spectra were detected. For C 1s spectra (Figure 5a), three typical peaks at 288.3, 286.3, and 284.7 eV can be assigned to sp^2-bonded C−N−C of the skeleton, the C−O group, and C−C of carbon contamination, respectively.[41] The N 1s spectrum could be deconvoluted into four peaks with binding energies at 404.3, 401.2, 399.4, and 398.7 eV (Figure 5b), which were attributed to the N−O, C−H−N, N−$(C)_3$, and C−N═C groups, respectively. A broad peak at 192.0 eV could be found in the B 1s level (Figure 5c), which is ascribed to the C-NB group. This is also evidence of the successful doping of B atoms in g-C_3N_4. The spectra of Ag 3d consists of two peaks with binding energies of 374.5 and 368.5 eV (Figure 5d), which are the standardized Ag $3d_{3/2}$ and Ag $3d_{5/2}$ levels of metallic Ag,[12] demonstrating that Ag NPs were successfully loaded on B-doped g-C_3N_4. The XPS spectra of g-C_3N_4 and B-g-C_3N_4 are shown in Figure S4 for comparison. The similar C 1s, N 1s, and B ls spectra for the three catalysts indicate that

https://doi.org/10.1021/acs.iecr.2c00152
Ind. Eng. Chem. Res. XXXX, XXX, XXX−XXX

the structure of the g-C_3N_4 support remains intact after doping with B and Ag.

ECR Activity Test. The ECR catalytic performances were first evaluated by LSV, as exhibited in Figure 6a. In the presence of CO_2 feed gas, the Ag-B-g-C_3N_4 catalyst showed apparently higher reduction current density in comparison with the other two samples, achieving a current density of -2.08 mA cm^{-2} at -0.8 V (vs RHE). The bare carbon paper and carbon black coated carbon paper were also tested as working electrodes but only exhibited a negligible weak current density (Figure S5). In N_2-saturated $KHCO_3$, the Faradaic currents can be attributed to HER, whereas it displayed a much higher current in CO_2-saturated $KHCO_3$ at the same potential (Figure 6b), indicting the catalytic activity of Ag-B-g-C_3N_4 for ECR. These results also suggested that Ag is the active center of the Ag-B-g-C_3N_4 electrocatalyst.

Constant potential electrolysis was performed by choosing the potential ranging from -0.5 V to -1.0 V (vs RHE) to study the ECR selectivity over the Ag-B-g-C_3N_4 catalyst. The resultant gaseous products were analyzed by online GC, while liquid products were analyzed by ^{1}H NMR spectroscopy. CO and H_2 were the only gaseous products with a total FE over 98% (Figure 6c). There is no liquid product found, as evidenced by ^{1}H NMR (Figure S6). The FE_{CO} of Ag-B-g-C_3N_4 increased first and then dropped with the increase of the applied potentials, achieving the maximum FE_{CO} of 93.2% at -0.8 V (vs RHE). It was worth mentioning that both pristine g-C_3N_4 and B-g-C_3N_4 did not produce CO but only H_2 under potentials between -0.5 V and -1.0 V (vs RHE). The bare carbon paper and carbon black coated carbon paper also only generate H_2. These results are consistent with DFT calculations that Ag-B-g-C_3N_4 catalysts show the lowest Gibbs free energy for *COOH generation, while B doping alone could not obviously decrease its Gibbs free energy. Therefore, it can be concluded that Ag NPs are the only active center for ECR to CO.

EIS was carried out at -0.8 V (vs RHE) to disclose the origin of the excellent reactivity of the Ag-B-g-C_3N_4 nanocomposite. The Nyquist plots of g-C_3N_4, B-g-C_3N_4, and Ag-B-g-C_3N_4 were displayed in Figure 6d. Notably, B atoms could effectively improve g-C_3N_4 electron transport due to the generation of the impurity levels. After loading Ag NPs, a much lower charge transfer resistance (R_{CT}) was achieved on Ag-B-g-C_3N_4, validating that the decoration of Ag NPs could enhance electron transportation between the catalyst and CO_2 molecules, thus the ECR capability. These results are in line with the DFT calculations that the electron accumulations at the Ag/B-g-C_3N_4 interface could improve electrical conductivity and promote electron transport.

The long-term stability of the Ag-B-g-C_3N_4 catalyst was examined at -0.8 V (vs RHE) (Figure 6e). Remarkably, the reduction current densities increased during the first hour and then remained stable at -2.08 mA cm^{-2} for 12 h. The corresponding FE_{CO} exhibited no obvious decay during the electrolysis process, indicating excellent stability of the catalyst for selective ECR to CO.

CONCLUSIONS

In this work, Ag NPs loaded on B-decorated g-C_3N_4 was chosen as the nanocomposite electrocatalyst system for ECR study. The ECR performance of the composite catalyst had been investigated through theoretical calculations and experimental work. DFT calculations showed that the Ag-B-g-C_3N_4 catalyst could remarkably decrease the adsorption free energy for *COOH generation. Besides, electron accumulation at the Ag-B-g-C_3N_4 interface could improve electrical conductivity and promote electron transport. The simulation results suggested that the introduction of B atoms and Ag NPs could improve the ECR performance of g-C_3N_4 effectively. Experimentally, we successfully prepared g-C_3N_4, B-g-C_3N_4, and Ag-B-g-C_3N_4 electrocatalysts, which was evidenced by XRD, TEM, and XPS characterizations. Only Ag-B-g-C_3N_4 could produce CO, indicating that Ag is the only active center. Meanwhile, EIS revealed that Ag atoms could promote electron transport. Consequently, the Ag-B-g-C_3N_4 catalyst with an average diameter of 4.95 nm exhibited a FE_{CO} of 93.2% at the potential of -0.8 V (vs RHE) with a total current density of -2.08 mA cm^{-2}. Moreover, the FE_{CO} and current density were maintained without obvious decay for an electrocatalysis of 12 h, demonstrating excellent stability. Therefore, the ECR mechanism on the g-C_3N_4 nanocomposite was understood by combined theoretical and experimental studies, which could offer insight of g-C_3N_4-based catalysts for other electrocatalytic applications.

ASSOCIATED CONTENT

Supporting Information

The Supporting Information is available free of charge at https://pubs.acs.org/doi/10.1021/acs.iecr.2c00152.

Optimized structures of g-C_3N_4, B-g-C_3N_4, and Ag-B-g-C_3N_4; possible active sites and free energy profiles for ECR to CO; TEM images of Ag NPs on B-g-C_3N_4 substrate and particle size distribution of Ag NPs; XPS spectra of C 1s and N 1s of g-C_3N_4 and B ls, C 1s, and N 1s of B-g-C_3N_4; LSV curves of bare carbon paper and carbon paper coated with carbon black; and ^{1}H NMR of possible liquid products (PDF)

AUTHOR INFORMATION

Corresponding Authors

Zhixin Yu − *Department of Energy and Petroleum Engineering, University of Stavanger, 4036 Stavanger, Norway;* orcid.org/0000-0003-2446-6537; Email: zhixin.yu@uis.no

Fengliu Lou − *Beyonder AS, 4033 Stavanger, Norway;* Email: fengliu@beyonder.no

Authors

Song Lu − *Department of Energy and Petroleum Engineering, University of Stavanger, 4036 Stavanger, Norway*

Yang Zhang − *Department of Energy and Petroleum Engineering, University of Stavanger, 4036 Stavanger, Norway; Beyonder AS, 4033 Stavanger, Norway*

Mohamed F. Mady − *Deaprtment of Chemistry, Bioscience and Environmental Engineering, University of Stavanger, 4036 Stavanger, Norway;* orcid.org/0000-0002-4636-0066

Wakshum Mekonnen Tucho − *Department of Mechanical and Structural Engineering and Material Science, University of Stavanger, 4036 Stavanger, Norway*

Complete contact information is available at: https://pubs.acs.org/10.1021/acs.iecr.2c00152

Notes

The authors declare no competing financial interest.

https://doi.org/10.1021/acs.iecr.2c00152
Ind. Eng. Chem. Res. XXXX, XXX, XXX−XXX

■ ACKNOWLEDGMENTS

This work was funded by the Norwegian Ministry of Education and Research. The computations were performed on resources provided by UNINETT Sigma2 - the National Infrastructure for High Performance Computing and Data Storage in Norway.

■ REFERENCES

(1) Chu, S.; Cui, Y.; Liu, N. The path towards sustainable energy. *Nat. Mater.* **2017**, *16*, 16−22.
(2) Quan, Y.; Zhu, J.; Zheng, G. Electrocatalytic reactions for converting CO_2 to value-added products. *Small Science* **2021**, *1*, 2100043.
(3) Agarwal, A. S.; Zhai, Y.; Hill, D.; Sridhar, N. The electrochemical reduction of carbon dioxide to formate/formic Acid: engineering and economic feasibility. *ChemSusChem* **2011**, *4*, 1301−1310.
(4) Pritchard, J.; Filonenko, G. A.; van Putten, R.; Hensen, E. J.; Pidko, E. A. Heterogeneous and homogeneous catalysis for the hydrogenation of carboxylic acid derivatives: history, advances and future directions. *Chem. Soc. Rev.* **2015**, *44*, 3808−3833.
(5) Ling, Y.; Ma, Q.; Yu, Y.; Zhang, B. Optimization strategies for selective CO_2 electroreduction to fuels. *Trans. Tianjin Univ.* **2021**, *27*, 180−200.
(6) Bushuyev, O. S.; De Luna, P.; Dinh, C. T.; Tao, L.; Saur, G.; van de Lagemaat, J.; Kelley, S. O.; Sargent, E. H. What should we make with CO_2 and how can we make it? *Joule* **2018**, *2*, 825−832.
(7) Zhu, D. D.; Liu, J. L.; Qiao, S. Z. Recent advances in inorganic heterogeneous electrocatalysts for reduction of carbon dioxide. *Adv. Mater.* **2016**, *28*, 3423−3452.
(8) Liang, Z.; Wang, H. Y.; Zheng, H.; Zhang, W.; Cao, R. Porphyrin-based frameworks for oxygen electrocatalysis and catalytic reduction of carbon dioxide. *Chem. Soc. Rev.* **2021**, *50*, 2540−2581.
(9) Wang, G.; Chen, J.; Ding, Y.; Cai, P.; Yi, L.; Li, Y.; Tu, C.; Hou, Y.; Wen, Z.; Dai, L. Electrocatalysis for CO_2 conversion: from fundamentals to value-added products. *Chem. Soc. Rev.* **2021**, *50*, 4993−5061.
(10) Li, Y.; Chen, C.; Cao, R.; Pan, Z.; He, H.; Zhou, K. Dual-atom Ag_2/graphene catalyst for efficient electroreduction of CO_2 to CO. *Appl. Catal. B: Environ.* **2020**, *268*, 118747.
(11) Zhang, H.; Li, J.; Xi, S. B.; Du, Y. H.; Hai, X.; Wang, J. Y.; Xu, H. M.; Wu, G.; Zhang, J.; Lu, J.; Wang, J. Z. A graphene-supported single-Atom FeN_5 catalytic site for efficient electrochemical CO_2 reduction. *Angew. Chem., Int. Ed.* **2019**, *58*, 14871−14876.
(12) Zhang, S.; Mo, Z.; Wang, J.; Liu, H.; Liu, P.; Hu, D.; Tan, T.; Wang, C. Ultra-stable oxygen species in Ag nanoparticles anchored on g-C_3N_4 for enhanced electrochemical reduction of CO_2. *Electrochim. Acta* **2021**, *390*, 138831.
(13) Mistry, H.; Reske, R.; Zeng, Z.; Zhao, Z. J.; Greeley, J.; Strasser, P.; Cuenya, B. R. Exceptional size-dependent activity enhancement in the electroreduction of CO_2 over Au nanoparticles. *J. Am. Chem. Soc.* **2014**, *136*, 16473−16476.
(14) Shi, R.; Guo, J.; Zhang, X.; Waterhouse, G. I. N.; Han, Z.; Zhao, Y.; Shang, L.; Zhou, C.; Jiang, L.; Zhang, T. Efficient wettability-controlled electroreduction of CO_2 to CO at Au/C Interfaces. *Nat. Commun.* **2020**, *11*, 3028.
(15) Yang, H.; Shang, L.; Zhang, Q.; Shi, R.; Waterhouse, G. I. N.; Gu, L.; Zhang, T. A universal ligand mediated method for large scale synthesis of transition metal single atom catalysts. *Nat. Commun.* **2019**, *10*, 4585.
(16) Back, S.; Yeom, M. S.; Jung, Y. Active sites of Au and Ag nanoparticle catalysts for CO_2 electroreduction to CO. *ACS Catal.* **2015**, *5*, 5089−5096.
(17) Li, H.; Wu, Y.; Li, C.; Gong, Y.; Niu, L.; Liu, X.; Jiang, Q.; Sun, C.; Xu, S. Design of Pt/T-ZrO_2/g-C_3N_4 efficient photocatalyst for the hydrogen evolution reaction. *Appl. Catal. B: Environ.* **2019**, *251*, 305−312.
(18) Kumar, A.; Xu, Q. Two-dimensional layered materials as catalyst supports. *ChemNanoMat* **2018**, *4*, 28−40.
(19) Cui, B.; Hu, B.; Liu, J.; Wang, M.; Song, Y.; Tian, K.; Zhang, Z.; He, L. Solution-plasma-assisted bimetallic oxide alloy nanoparticles of Pt and Pd embedded within two-dimensional $Ti_3C_2T_X$ nanosheets as highly active electrocatalysts for overall water splitting. *ACS Appl. Mater. Interfaces* **2018**, *10*, 23858−23873.
(20) Kuang, S.; Li, M.; Xia, R.; Xing, L.; Su, Y.; Fan, Q.; Liu, J.; Hensen, E. J. M.; Ma, X.; Zhang, S. Stable surface-anchored Cu nanocubes for CO_2 electroreduction to ethylene. *ACS Appl. Nano Mater.* **2020**, *3*, 8328−8334.
(21) Zheng, Y.; Jiao, Y.; Zhu, Y.; Cai, Q.; Vasileff, A.; Li, L. H.; Han, Y.; Chen, Y.; Qiao, S. Z. Molecule-level g-C_3N_4 coordinated transition metals as a new class of electrocatalysts for oxygen electrode reactions. *J. Am. Chem. Soc.* **2017**, *139*, 3336−3339.
(22) Yan, Q.; Huang, G. F.; Li, D. F.; Zhang, M.; Pan, A. L.; Huang, W. Q. Facile synthesis and superior photocatalytic and electrocatalytic performances of porous B-doped g-C_3N_4 nanosheets. *J. Mater. Sci. Technol.* **2018**, *34*, 2515−2520.
(23) Sun, J.; Bian, J.; Li, J.; Zhang, Z.; Li, Z.; Qu, Y.; Bai, L.; Yang, Z. D.; Jing, L. Efficiently photocatalytic conversion of CO_2 on ultrathin metal phthalocyanine/g-C_3N_4 heterojunctions by promoting charge transfer and CO_2 activation. *Appl. Catal. B: Environ.* **2020**, *277*, 119199.
(24) Guo, S.; Zhao, S. Q.; Wu, X. Q.; Li, H.; Zhou, Y. J.; Zhu, C.; Yang, N. J.; Jiang, X.; Gao, J.; Bai, L.; Liu, Y.; Lifshitz, Y.; Lee, S. T.; Kang, Z. H. A Co_3O_4-Cdots-C_3N_4 three component electrocatalyst design concept for efficient and tunable CO_2 reduction to syngas. *Nat. Commun.* **2017**, *8*, 1828.
(25) Wang, H.; Sun, T.; Chang, L.; Nie, P.; Zhang, X.; Zhao, C.; Xue, X. The g-C_3N_4 nanosheets decorated by plasmonic Au nanoparticles: A heterogeneous electrocatalyst for oxygen evolution reaction enhanced by sunlight illumination. *Electrochim. Acta* **2019**, *303*, 110−117.
(26) Jiao, Y.; Zheng, Y.; Smith, S. C.; Du, A.; Zhu, Z. Electrocatalytically switchable CO_2 capture: first principle computational exploration of carbon nanotubes with pyridinic nitrogen. *ChemSusChem* **2014**, *7*, 435−441.
(27) Zheng, Y.; Jiao, Y.; Chen, J.; Liu, J.; Liang, J.; Du, A. J.; Zhang, W. M.; Zhu, Z. H.; Smith, S. C.; Jaroniec, M.; Lu, G. Q.; Qiao, S. Z. Nanoporous graphitic-C_3N_4@carbon metal-free electrocatalysts for highly efficient oxygen reduction. *J. Am. Chem. Soc.* **2011**, *133*, 20116−20119.
(28) Zhang, L.; Mao, F.; Zheng, L. R.; Wang, H. F.; Yang, X. H.; Yang, H. G. Tuning metal catalyst with metal-C_3N_4 interaction for efficient CoO_2 electroreduction. *ACS Catal.* **2018**, *8*, 11035−11041.
(29) Chen, J.; Wang, Z.; Lee, H.; Mao, J.; Grimes, C. A.; Liu, C.; Zhang, M.; Lu, Z.; Chen, Y.; Feng, S. P. Efficient electroreduction of CO_2 to CO by Ag-decorated S-doped g-C_3N_4/CNT nanocomposites at industrial scale current density. *Mater. Today Phys.* **2020**, *12*, 100176.
(30) Lu, S.; Li, C.; Li, H. H.; Zhao, Y. F.; Gong, Y. Y.; Niu, L. Y.; Liu, X. J.; Wang, T. The effects of nonmetal dopants on the electronic, optical and chemical performances of monolayer g-C_3N_4 by first-principles study. *Appl. Surf. Sci.* **2017**, *392*, 966−974.
(31) Wei, B.; Wang, W.; Sun, J.; Mei, Q.; An, Z.; Cao, H.; Han, D.; Xie, J.; Zhan, J.; He, M. Insight into the effect of boron doping on electronic structure, photocatalytic and adsorption performance of g-C_3N_4 by first-principles study. *Appl. Surf. Sci.* **2020**, *511*, 145549.
(32) Kresse, G.; Furthmüller, J. Efficiency of ab-initio total energy calculations for metals and semiconductors using a plane-wave basis set. *Comput. Mater. Sci.* **1996**, *6*, 15−50.
(33) Kresse, G.; Furthmüller. Efficient iterative schemes for ab initio total-energy calculations using a plane-wave basis set. *Phys. Rev. B* **1996**, *54*, 11169−11186.
(34) Perdew, J. P.; Burke, K.; Ernzerhof, M. Generalized gradient approximation made simple. *Phys. Rev. Lett.* **1996**, *77*, 3865−3868.
(35) Kresse, G.; Joubert, D. From ultrasoft pseudopotentials to the projector augmented-wave method. *Phys. Rev. B* **1999**, *59*, 1758−1775.

https://doi.org/10.1021/acs.iecr.2c00152
Ind. Eng. Chem. Res. XXXX, XXX, XXX−XXX

(36) Grimme, S.; Antony, J.; Ehrlich, S.; Krieg, H. A consistent and accurate ab Initio parametrization of density functional dispersion correction (DFT-D) for the 94 Elements H-Pu. *J. Chem. Phys.* **2010**, *132*, 154104.
(37) Nørskov, J. K.; Rossmeisl, J.; Logadottir, A.; Lindqvist, L.; Kitchin, J. R.; Bligaard, T.; Jónsson, H. Origin of the overpotential for oxygen reduction at a fuel-cell cathode. *J. Phys. Chem. B* **2004**, *108*, 17886−17892.
(38) Thaweesak, S.; Lyu, M.; Peerakiatkhajohn, P.; Butburee, T.; Luo, B.; Chen, H.; Wang, L. Two-dimensional g-C_3N_4/$Ca_2Nb_2TaO_{10}$ nanosheet composites for efficient visible light photocatalytic hydrogen evolution. *Appl. Catal. B: Environ.* **2017**, *202*, 184−190.
(39) Thorat, N.; Yadav, A.; Yadav, M.; Gupta, S.; Varma, R.; Pillai, S.; Fernandes, R.; Patel, M.; Patel, N. Ag loaded B-doped-g-C_3N_4 nanosheet with efficient properties for photocatalysis. *J. Environ. Manage* **2019**, *247*, 57−66.
(40) Hong, J.; Xia, X.; Wang, Y.; Xu, R. Mesoporous carbon nitride with in situ sulfur doping for enhanced photocatalytic hydrogen evolution from water under visible light. *J. Mater. Chem.* **2012**, *22*, 15006−15012.
(41) Caux, M.; Fina, F.; Irvine, J. T. S.; Idriss, H.; Howe, R. Impact of the annealing temperature on Pt/g-C_3N_4 structure, activity and selectivity between photodegradation and water splitting. *Catal. Today* **2017**, *287*, 182−188.

https://doi.org/10.1021/acs.iecr.2c00152
Ind. Eng. Chem. Res. XXXX, XXX, XXX−XXX